Effects of manufacturing parameters, heat treatment, and machining on the physical and mechanical properties of 13Cr10Ni1·7Mo2Al0·4Mn0·4Si steel processed by laser powder bed fusion

Shahriar Afkhami [a,*], Vahid Javaheri [b], Edris Dabiri [a], Heidi Piili [c], Timo Björk [a]

[a] *Laboratory of Steel Structures, LUT University, Lappeenranta, 53850, Finland*
[b] *Materials and Mechanical Engineering, University of Oulu, 90014, Finland*
[c] *Laboratory of Laser Materials Processing and Additive Manufacturing, LUT University, Lappeenranta, 53850, Finland*

ARTICLE INFO

ABSTRACT

This study investigates the effects of build orientations, heat treatment, and mechanical machining (as processing and post-processing factors) on the microstructure, quasi-static mechanical properties, strain hardening, notch toughness, and residual stress of additive manufactured 13Cr10Ni1·7Mo2Al0·4Mn0·4Si maraging stainless steel, known commercially as CX. The material investigated in this research was processed using the laser powder bed fusion (L-PBF) method as the additive manufacturing process. The results show that stainless steel CX had an anisotropic behavior under quasi-static tensile loads in its as-built condition. However, heat treatment significantly increased the strength of the material and eliminated the anisotropy in the strength levels. In addition, building orientation did not significantly affect the microstructure, hardness, and notch toughness. Further, retained austenite proved to have a role in determining the ductility and strain hardening of CX. Finally, the heat treatment utilized in this study proved to be effective in improving the mechanical properties employing shorter times and lower temperatures compared to the treatments used in other studies from the literature.

1. Introduction

Additive manufacturing (AM) of metals expands its influence on industry and construction by providing these application areas with new design and material modification possibilities. However, to satisfy newly developed ideas, these domains demand new materials with better characteristics, e.g., higher strength, toughness, ductility, and corrosion resistance. Consequently, new metals are introduced for AM to make additively manufactured components fit the expectations. However, AM metals are highly prone to microstructural heterogeneities, refined grain structures, high dislocation densities, residual stresses, anisotropic properties, and nonequilibrium phases compared to their conventionally manufactured counterparts. Thus, the behavior and characteristics of AM metals must be thoroughly understood so that these materials can be used in a wide variety of applications with a satisfying level of reliability and confidence [1,2].

One of the newly developed metals for the Laser-powder bed fusion (L-PBF) technique, as a frequently utilized AM method for industrial applications, is the 13 wt% Cr precipitation hardening martensitic stainless steel with the commercial name CX by EOS GmbH. As a precipitation hardening (PH) steel, CX seems to be a good candidate and economical choice to replace more expensive alloys, e.g., Ti–6Al–4V, for heavy-duty applications that require a combination of high strength and corrosion resistance [2–4]. Thus, this metal can be used in the aerospace, marine, and automobile industries, die production, petrochemical plants, nuclear reactors, and energy sections due to its excellent corrosion resistance and enhanced mechanical properties [1,5].

Based on the alloying elements, there is a variety of PH martensitic stainless steels available for AM. For example, steels such as 17-4PH and 15-5PH rely on copper as their primary strengthening element for the aging treatment. In addition, the majority of commonly used AM maraging steels, e.g., 1.2709 (commercially known as MS1), get strengthened by precipitation of a mixture of intermetallic particles such as Fe_2Mo, Fe_7Mo_6, and especially Ni_3Ti [6]. However, these particles cannot maintain alloy strength under moderate to high working temperatures. Consequently, to overcome this limitation, in the new generation of AM maraging steels, e.g., Uddeholm Corrax and EOS CX, ordered β-NiAl particles, as the result of aging treatment, contribute to

strengthening the materials [5,7].

For the sake of comparison, it could be said that the characteristics of these newly developed AM steels, including CX, are similar to those of conventional PH 13-8Mo steel. Consequently, these steels have lower Ni contents to become more thermally stable and utilize highly coherent β-NiAl particles with a CsCl superlattice structure and lattice parameters close to those of BCC iron to maximize the effectiveness of the strengthening mechanism [1–3,5,8]. Such a good combination of mechanical and physical properties, e.g., strength and corrosion resistance, suggests various potential applications for CX processed by the L-PBF technique (L-PBF CX). Therefore, this material has been the subject of numerous studies recently. According to these investigations, L-PBF CX has a ductile martensitic microstructure in its as-built condition, providing a good combination of strength, ductility, and corrosion resistance. Furthermore, heat-treated L-PBF CX achieves ultra-high strength levels accompanied by good corrosion resistance [9–15].

Most studies related to L-PBF CX have not used the recently optimized and less energy- and time-consuming heat treatment developed by EOS on the material. Thus, the efficiency of the optimized heat treatment has yet to be discovered. Furthermore, some mechanical properties of L-PBF CX, such as its hardening behavior, toughness, and fatigue performance, require further research, and the correlation between the microstructural features and these mechanical properties should be thoroughly understood. Furthermore, research on L-PBF CX has been confined to studying a limited number of individual parameters, e.g., heat input, laser beam characteristics, building orientation, and their effects on the material. Thus, a more comprehensive study to consider the simultaneous effects of processing and post-processing parameters has critically been required. Finally, the development of residual stress in L-PBF CX and the effects of heat treatment or other post-processing methods on the residual stress require investigation.

Considering the mentioned knowledge gaps and scientific niches about L-PBF CX, this study aimed to investigate this material. In addition, it intended to look into the quasi-static mechanical properties, strain hardening behavior, and notch toughness of L-PBF CX. Furthermore, correlations between the microstructural features and mechanical properties are introduced and discussed based on the achieved results. Next, the generation of residual stress in the material and its influence on the heat-treated microstructure were also investigated. Finally, the influence of building orientation (as a processing parameter), heat treatment (as a post-processing procedure), and surface condition (mechanical machining as a post-processing option) in conjunction with the material properties were studied to understand L-PBF CX behavior further.

2. Materials and methods

Fresh gas-atomized CX stainless steel powder from EOS GmbH was used as the raw material in this study. The chemical composition of the powder is presented in Table 1. The specimens were manufactured using an EOS M 290 machine, equipped with a 400 W Yb-Fiber laser, under optimized parameters provided by the manufacturer. These parameters were also used in some previous studies on CX using the same AM machine to achieve fully dense parts [1,3–5,12,15–17]. The samples were manufactured along both the horizontal and vertical orientations to investigate the effects of the building direction (BD). Consequently, the BD and loading axis (LA) in mechanical tests were normal in the horizontal and parallel in the vertical samples. Further detail on the geometry and dimensions of the specimens are available in Supplementary

Fig. 1 and Fig. 2.[1]

Once manufactured, horizontal and vertical specimens were subdivided into two groups based on their post-processing: as-built (without post-processing) and heat-treated. Subsequently, heat-treated specimens were post-processed following this procedure: solution annealing at 850 °C for 30 min, then air cooling to room temperature (20 °C) and aging for 120 min at 525 °C, and, again, air cooling to room temperature (Supplementary Fig. 3). In other studies, as examples, the solution annealing was performed for 60 min at 1000 °C and 900 °C in Refs. [10, 14], respectively. Furthermore, the aging step lasted for 180 min at 530 °C in [14]. However, the heat treatment used in this study was optimized following the instruction provided by the powder manufacturer [16].

The heat treatment was planned to reach the best material performance in a shorter time and by consuming less energy than the treatments used in the preceding investigations available in the literature. Consequently, the duration of the solution annealing and aging treatments were shortened at least 50% and 30%, respectively, compared to the procedures used in, e.g. Refs. [2,5,10], and [14]. The heat treatment was carried out in a sealed furnace under the pure argon atmosphere to avoid any unwanted reaction in the material. In addition, one horizontal and one vertical sample were subjected to dilatometry with a Gleeble 3500 thermomechanical simulator to investigate the phase transformations triggered by the heat treatment.

Densities of the manufactured samples were measured by the Archimedes method using acetone as the immersion medium to increase the accuracy of the measurements. In addition, the measurements were repeated three times to ensure the reliability and repeatability of the results [18,19]. Cross-sectional images of the polished and unetched surfaces from eight different specimens were obtained using optical microscopy to analyze the shape, size, and distribution of the defects. The image analysis was carried out via the ImageJ software. Finally, the relative density of the material was estimated based on the data from both the Archimedes and image analysis approaches to verify the acceptable quality of the manufactured specimens.

For the microstructural analysis, 10 mm × 10 mm × 10 mm cuboid specimens were mounted in epoxy resin, ground and polished sequentially, and were etched with Kalling's reagent for 15 s [20]. Subsequently, scanning electron microscopy (SEM) was performed using a SU3500 (Hi-Tech Instruments) equipped with an energy-dispersive X-ray spectroscopy (EDS) probe for elemental analysis. In addition, higher magnification microstructural investigations were carried out using a JEOL JSM-7900F field emission scanning electron microscope (FE-SEM) equipped with an EDS probe. Finally, a ZEISS Sigma FE-SEM was also used for electron backscatter diffraction (EBSD) measurements to investigate microstructural phases and textures. The EBSD measurements were carried out using an accelerating voltage of 15 kV, a working distance of 15 mm, and a scanning step of 0.2 μm. Data achieved from the EBSD approach were analyzed with TSL software.

To investigate the effects of residual stress on the microstructure of heat-treated CX, one horizontal and one vertical 10 mm × 10 mm × 100 mm samples were bent 45° from the middle of their lengths to cause tensile residual stress on one side and compressive residual stress on the other side of the specimens. For further clarification, the visual presentations of the bent specimens are available in Section 3.2. Then, the bent specimens were heat treated according to the procedure described earlier in this section and subjected to SEM and EBSD microstructural analysis. In addition, the residual stress of the samples, consisting of the bent and normal ones, were measured using a Stresstech XSTRESS G2R X-ray diffractometer. Finally, the Vickers hardness values of the specimens were measured with a Struers DuraScan 70 by applying 3 Kgf for 10 s.

As shown in Table 2, for the quasi-static tensile and notch toughness

Table 1
Chemical composition of the powder [16].

Element	Fe	Cr	Ni	Mo	Al	Mn	Si	C
Max wt%	Bal.	13.00	10.00	1.70	2.00	0.40	0.40	0.05
Min wt%	Bal.	11.00	8.40	1.10	1.20	–	–	–

---

[1] Supplementary data are available as an open access article published in the Journal of Data in Brief and linked to the current article.

Charpy tests, samples were divided into subgroups based on their manufacturing and post-processing conditions to investigate the synergic effects of heat treatment, surface condition, and BD. Surface quality and roughness values we measured with a KEYENCE VE-3200 3D measuring microscope. Quasi-static tensile tests were performed with a Galdabini Quasar 600 machine at room temperature and under a constant strain rate of $0.001 \ s^{-1}$. In addition, an ARAMIS digital image correlation (DIC) system was utilized to measure the local strain values, fracture displacements, and true stress and logarithmic strain values. For the tensile tests, circular samples with 6 mm diameter in their gauge areas were manufactured (dimensions according to ASTM E8 [21], shown in Supplementary Fig. 1). Specimens with the machined surface were subjected to 0.5 mm material removal to achieve their target surface quality. Each test was repeated at least two times for each group in Table 2 to ensure the repeatability of the results.

Finally, Charpy tests were conducted at room temperature to measure the notch toughness of the specimens with different BDs. Specimens were manufactured with standard dimensions of 10 mm × 10 mm × 55 mm per ASTM E23 [22], as shown in Supplementary Fig. 1. The notches were manufactured by the L-PBF technique (without further machining), so the results represent the AM material with the raw surface. The fractured surface of each sample was analyzed with the KEYENCE VR-3200 3D microscope to measure their shear fracture appearances (SFA) accurately. The SFA represents the ductile to brittle fracture ratio of broken specimens and can be used as a qualitative criterion to compare the fracture mechanisms of the Charpy samples [19]. The notches were placed on the top side of the vertical specimens to avoid the stair-case effect inside the notches, as shown in Supplementary Fig. 2.

3. Results

According to the results from the Archimedes approach and considering its accuracy for dense AM metals, the relative density of the material was estimated to be 99.9% ± 0.1% ($\approx 7.7 \ g/cm^3$) [16,18]. After density measurements, areas of $1200 \times 800 \ \mu m^2$ from different specimens were analyzed to determine their defect distributions and achieve their statistical data. For this purpose, two specimens were selected from each sample group (Table 2), one representing the building plane and the other representing the scanning plane. According to the results, the majority of the defects ($\geq 80\%$) were spherical (porosities with circularity values higher than 0.5) with average diameters smaller than five μm (defect areas $\leq 100 \ \mu m^2$). In addition, the distribution of the defects was relatively uniform, and no sign of clustering was detected during the visual inspection. Furthermore, building direction and the heat treatment did not significantly affect the type, size, and distribution of the defects. Graphical representations of the defect size and distribution data are available in Supplementary Fig. 4.

3.1. Microstructural analysis and phase transformations

Microstructural features of the as-built specimens are presented in

Table 2
Summary of the specimen types investigated in this research.

| Sample group	Surface condition	BD	Post-processing
Machined horizontal (as-built)	Machined	Horizontal	As-built
Machined horizontal (heat-treated)	Machined	Horizontal	Heat-treated
Raw vertical (as-built)	Raw	Vertical	As-built
Raw vertical (heat-treated)	Raw	Vertical	Heat-treated
Machined vertical (as-built)	Machined	Vertical	As-built
Machined vertical (heat-treated)	Machined	Vertical	Heat-treated

Fig. 1. According to the figure, both the horizontal and vertical samples consisted of a mixture of martensitic features with lath (LM) or dendritic (DM) morphologies in their as-built condition. LM had a smooth appearance in the SEM images, while DM manifested as a cellular/dendritic feature [2,3]. In Fig. 1, some examples of LM and DM are marked by red and green highlights, respectively (further SEM images of the samples are available in Supplementary Figure 5 and Fig. 6). Finally, according to the inverse pole figures (IPF) and phase maps from the EBSD data, both horizontal and vertical samples were mixtures of martensite and retained austenite (RA) with generally weak crystallographic textures. The revealed RA islands were typically scattered along the high-angle grain boundaries (HAGB). As an example, EBSD data of the horizontal specimens are presented in Fig. 2. Further, EBSD data of the vertical samples are available in Supplementary Fig. 7.

Regarding the crystallographic texture, orientation distribution function (ODF) maps (Supplementary Fig. 8) showed weak cube {001}<100> and copper {112}<111> components belonging to the background microstructure (martensite in the building plane) with maximum intensities of 2.7 and 3.7 in the horizontal and vertical samples, respectively. Considering the low maximum intensity values and visual IPF data from the as-built specimens, the nature of all as-built samples, consisting of the horizontal and vertical ones, was considered weakly textured with a weak <111> tendency along the BD. In addition, austenite islands arranged along the HAGBs showed a weak <110> texture in both the horizontal and vertical specimens. However, these crystallographic textures were more pronounced in the vertical samples.

Numerical data achieved from the grain boundary and phase maps of the as-built samples are summarized in Table 4. From the EBSD data, LAGBs are divided into two groups of boundaries, one with misorientation angles between 1° and 5° and the other one with 5°–15°. Although all LAGBs represent martensitic laths, boundaries with misorientations close to the lower threshold (i.e., 1°–5°) in this study are attributed to the dislocations trapped inside the laths [1,2,5,10,13]. Thus, these LAGBs can also be used as a qualitative tool to compare dislocation densities. Finally, the average grain sizes of the samples measured based on the HAGBs are presented in Fig. 3. It should be noted that the HAGBs in the EBSD analysis were defined as the boundaries with misorientation angles between 15° and 60°. Consequently, these boundaries represent martensitic blocks, packets, and prior austenite grains (PAG) altogether. Hence, the grain size analysis carried out based on such boundaries refers to block size as an effective grain size in martensitic steels [2,23]. As shown in Fig. 3, the vertical (as-built) samples had a slightly higher fraction of larger grains than the horizontal (as-built) specimens. This difference was increased after the heat treatment.

Regarding the heat treatment procedure, expected microstructural transformations through the heating cycle were identified using ThermoCalc software (Fig. 4 a). According to Fig. 4(b), by heating the as-built L-PBF CX, its precipitates started to dissolve at ≈ 550 °C, and austenitization occurred at ≈ 750 °C for both the horizontal and vertical specimens. However, austenitization caused higher dilation in the vertical specimen, indicating a faster austenitization rate than the horizontal sample. Therefore, austenite grains in the vertical samples had more time to grow. In addition, martensite start (Ms) temperature was slightly lower for the horizontal samples. Finally, precipitation of the strengthening particles occurred for both the horizontal and vertical specimens during their final aging treatment.

Microstructures of the heat-treated specimens consisted of a mixture of LM and DM, regardless of the building orientation, as shown in Fig. 5. However, the LM to DM ratio was higher in the heat-treated L-PBF CX than in its as-built condition. Additionally, the presence of austenite in the heat-treated samples was confirmed by EBSD analysis, as shown in Fig. 2 (and Supplementary Fig. 7). According to the EBSD analysis, the crystallographic texture of the specimens became even weaker after the heat treatment. Numerical data from the EBSD results of the heat-treated samples are also presented in Table 4. According to the data, heat treatment resulted in a significant increase in the HAGBs to LAGBs ratio
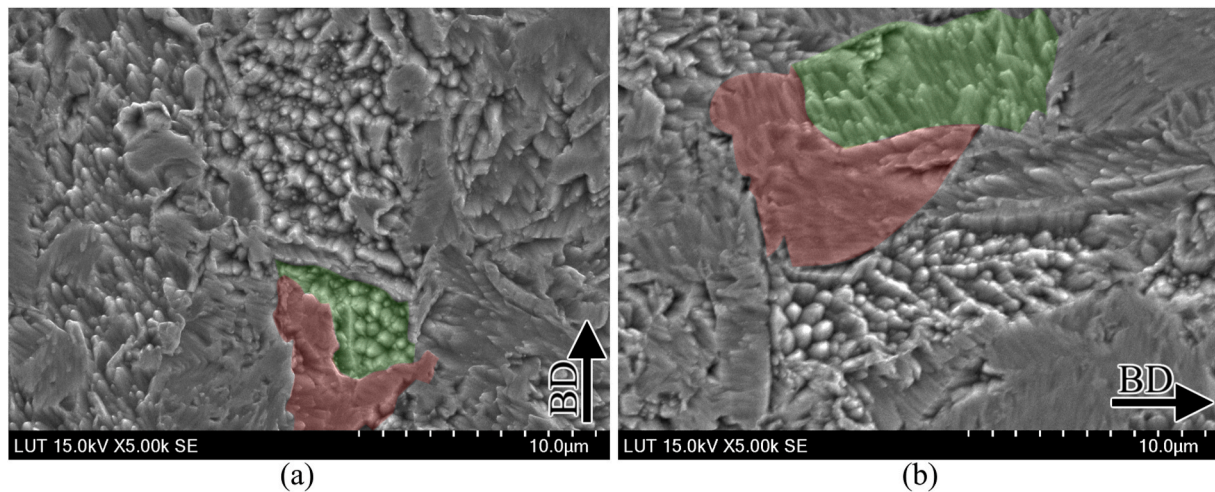
Fig. 1. High-magnification SEM micrographs of the as-built samples in their building planes and according to their BDs: (a) horizontal and (b) vertical.

and a drastic decrease in the total length of LAGBs with 1°–5° misorientations. In addition, the heat treatment increased the effective grain size of L-PBF CX, and the grain coarsening was more prominent in the vertical specimens, as shown in Fig. 3.

After the EBSD analysis, the microstructures of the heat-treated specimens were further investigated in higher magnifications via FE-SEM, and two types of particles were identified in the heat-treated L-PBF CX. As shown in Fig. 6 and according to EDS analysis, the first type, marked by a white arrow accompanied with the EDS data, was scarcely scattered aluminum oxides. These rare particles can be considered inclusions inherited from the raw powder, AM machine, or heat treatment furnace. The second group was uniformly distributed nano-sized precipitates, shown as white dots in higher magnification and contrast in the subset on the left side of Fig. 6. These nanoparticles were too small (<10 nm) to be analyzed via FE-SEM and EDS (e.g., Supplementary Fig. 9). However, according to the literature, they can be identified as coherent β-NiAl strengthening precipitates from the aging treatment [2, 14].

3.2. Surface roughness, residual stress, and hardness measurements

The surface roughness values of the specimens are presented in Table 5. According to the results, the heat treatment or BD did not alter the surface quality. However, mechanical machining improved the average surface quality (Ra values). Furthermore, the most significant improvement due to the machining was in the Rz values representing the maximum height differences from the topographical features of the surfaces. Hence, machining had a considerable role in removing the most critical surface defects from the AM components. In addition, This mechanical treatment caused compressive residual stress on the samples.

Regarding the residual stress, the values of the as-built and heat-treated samples are shown in Fig. 7 (a) and (b), respectively. The reported values were measured along the longitudinal (loading) axis of the specimens, regardless of their building orientation. Unlike the other sets having compressive residual stress, the raw vertical (as-built) specimens had tensile residual stress values. In addition, the tensile residual stress increased from the bottom to the top of these specimens. According to Fig. 7(b), the heat treatment significantly decreased and normalized the residual stress values in all the specimens, regardless of their BD or surface condition.

One horizontal sample and a vertical specimen were bent 45° and heat treated to investigate the effects of residual stress on the phase transformations. Before the heat treatment, the residual stress values of the bent samples were measured, and the results are presented in Fig. 7

(c). As shown in this figure, the bending process caused compressive residual stress on the outer curvatures, while tensile residual stress was present on the inside curvatures of the specimens, regardless of the building orientation. The results belonging to the EBSD analysis performed after the heat treatment of the bent samples are presented in Table 6. Comparing these results with each other and the data from Table 4 shows that residual stress, regardless of its nature, type, and direction, did not significantly alter the post-heat treatment microstructure.

Finally, the hardness values of the specimens are presented in Table 7. According to the hardness measurements, BD did not have a significant effect on this property. In addition, the hardness values were similar in the building and scanning planes of the samples. However, the heat treatment caused a considerable increase (≈50%) in the average hardness of L-PBF CX, regardless of its BD. The increase rates were also similar in the building and scanning planes. Finally, regarding the effect of residual stress on the post-heat treatment hardness, the bent samples, after the heat treatment, also had hardness values similar to those of other specimens. This observation was valid for either side of these samples (their inside and outer curvatures). Thus, regardless of its nature, type, and direction, residual stress did not significantly alter the hardness increase resulting from the heat treatment.

3.3. Quasi-static tensile test

The engineering stress-strain curves and the mechanical properties of L-PBF CX are presented in Fig. 8 and Table 8, respectively. Typically, increased strength values are accompanied by decreased ductility when comparing as-built horizontally-made AM metals to their vertically manufactured counterparts [24–26]. However, this trade-off was not valid for L-PBF CX, and, according to the results, the horizontal samples had higher strength and elongation values than the verticals. In addition, machining did not significantly affect the strength, but it decreased the elongation to failure. Next, the true stress-logarithmic strain curves of the specimens were plotted via the DIC technique to investigate the behavior of L-PBF CX and its strain hardening during plastic deformation. These curves were plotted based on the weakest points of the specimens (e.g., Supplementary Figure 10). According to the results (visually available in Supplementary Figure 11), the as-built vertical specimens had a three-stage strain hardening (i.e., a sharp drop to a gradual increase and then a gradual decline), unlike the rest of the samples having a two-stage hardening behavior (i.e., a sharp drop followed by a gradual and stable decline). Finally, the heat treatment increased strength levels of both horizontal and vertical specimens but decreased their ductility values, and the rate of increase in strength and
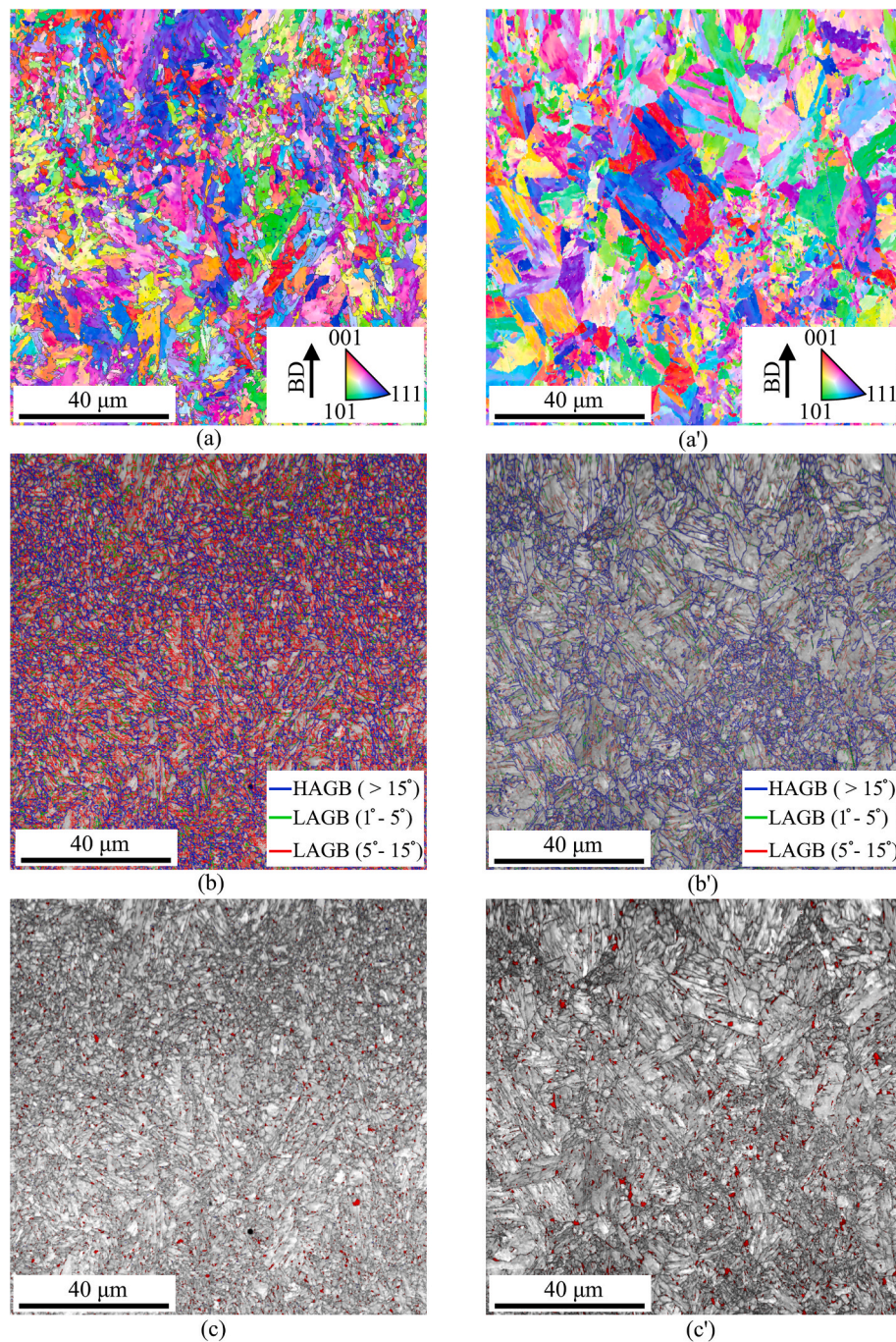
Fig. 2. Results of the EBSD analysis for the horizontal specimens from their building plane: (a, a') IPF maps, (b, b') grain boundary maps, and (c, c') image quality (IQ) maps of the (left) as-built and (right) heat-treated samples (RA islands are superimposed on the IQ maps as red spots, and the remaining areas are martensitic). More details on the fractions of RA and grain boundaries are available in Table 4.

Table 3

Void distributions in the manufactured samples.

| BD and post-processing	Area fraction of the voids in the building plane (%)	Area fraction of the voids in the scanning plane (%)
Horizontal (as-built)	0.1%	0.8%
Horizontal (heat-treated)	0.1%	0.4%
Vertical (as-built)	0.4%	0.7%
Vertical (heat-treated)	0.1%	0.5%

decrease in ductility was independent of the surface condition or BD.

3.4. Notch toughness (charpy) test

The notch toughness values of L-PBF CX and its SFAs, based on the BDs and post-processing conditions, are presented in Table 9 (visual presentations of the SFAs are available in Supplementary Figure 12). According to the results, the notch toughness of the horizontally made L-PBF CX was slightly higher than the vertical samples, both in the as-built and heat-treated conditions. Furthermore, the heat treatment resulted in a significant decrease (≈80%) in the notch toughness of L-PBF CX, regardless of its BD. According to the SFA values, horizontal and vertical

Table 4
Numerical data from the EBSD analysis.

BD and post-processing	LAGBs fraction (1° - 5°)	LAGBs fraction (5° - 15°)	HAGBs fraction (> 15°)	Area fraction of austenite	Area fraction of martensite
Horizontal (as-built)	58.6% (3.9 cm)	8.4% (0.6 cm)	33.0% (2.2 cm)	2.8%	97.2%
Horizontal (heat-treated)	26.4% (0.9 cm)	13.4% (0.4 cm)	60.2% (2.0 cm)	3.8%	96.2%
Vertical (as-built)	58.5% (3.8 cm)	7.7% (0.5 cm)	33.8% (2.2 cm)	1.8%	98.2%
Vertical (heat-treated)	26.7% (0.8 cm)	14.6% (0.4 cm)	58.7% (1.8 cm)	3.0%	97.0%
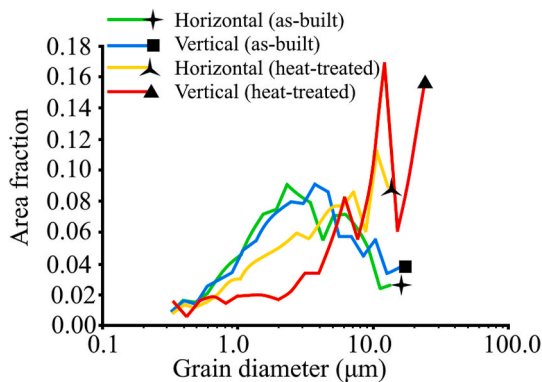
Fig. 3. Grain size distributions.

samples had similar levels of ductile fractures under the impact load, regardless of their post-processing condition. However, the heat-treated specimens experienced more brittle failures significantly since they had extremely lower SFA values than their as-built types.

4. Discussion

Porosities with diameters smaller than five μm are commonly considered hereditary to L-PBF of metals due to the gas entrapment originating from the raw powder. According to the literature, these isolated voids are relatively harmless to the mechanical properties of AM metals as long as, in most cases, their relative density is higher than 99%, and no porosity clustering is present throughout the microstructure [19,24,26]. According to the data from Supplementary Fig. 4, the distribution of defects was uniform in L-PBF CX, and there was no noticeable difference between the specimens, regardless of their BD or post-processing condition. Considering these observations and the data summarized in Table 3, the quality of the manufactured samples was considered acceptable for performing mechanical tests and microstructural analysis.

4.1. Microstructural features

The microstructure of AM maraging steels in their as-built condition is expected to be a combination of lath and dendritic martensite, considering the complex thermal cycles associated with the L-PBF technique consisting of repetitive rapid heating and cooling courses [7]. As a precipitation hardening stainless steel with a chemical composition close to AM low-carbon maraging steels, L-PBF CX was also expected to have such microstructural features, as shown in Fig. 1, since CX is more similar to low-carbon maraging AM steels, e.g., EOS MS1, than traditional precipitation hardening AM steels. The coexistence of dendritic and lath morphologies in the as-built L-PBF CX, and other steels similar

to it, can be attributed to different local thermal cycles these materials undergo during their AM process [3,7].

Subgrain morphologies in metals processed by techniques associated with rapid thermal cycles, e.g., welding or AM, rely on the ratio of the temperature gradient (G) to the crystallographic growth rate (R), and low G to R ratios result in dendritic features [8,27]. Considering the asymmetrical shape of the melt pools in L-PBF and their high depth to width ratios, this dependency encourages dendrite formation, especially in the bottom center of the melt pools due to the lower G/R values in these areas. Thus, although L-PBF CX is highly prone to martensite formation through its solidification, the formed martensite is dendritic instead of lath-shaped in some areas due to the low local G/R. Furthermore, some relatively large and elongated microstructural features with HAGBs in the as-built specimens (e.g., Fig. 2(a)) are direct results of epitaxial growth along the melt pool boundaries during the L-PBF process [1,4,8,10,11,13].

The presence of RA at room temperature in the as-built samples is due to the incomplete austenite to martensite transformation during the cooling-down course of the laser scans. This local stabilization and incomplete transformation of the austenite along the HAGBs can result from the microsegregation of alloying elements in these locations. Consequently, the weak <111>/<110> relationship detected between the austenitic islands and martensitic backgrounds in the as-built samples corresponds to the common Kurdjumov-Sachs relationship between the adjacent austenite and martensite structures [8]. These weak final textures of the as-built samples resulted from two consecutive transformations in solidifying L-PBF CX. At first, according to Fig. 4(a), the melt pool solidified as δ ferrite. Next, δ ferrite to austenite transformation resulted in austenite with a <110> ∥ BD texture. Finally, austenite to martensite transformation occurred. Although the last transformation was expected to result in a <111> ∥ BD texture, the final texture was semi-random (with a weak <111> tendency). This texture weakening is due to the numerous arbitrary and stochastic formations of different martensite variants in each austenite grain during the rapid cooling stage of each L-PBF pass [7]. Regarding the heat-treated CX, the presence of elongated Lath-like austenitic morphologies along some LAGBs, beside austenitic islands along HAGBs (Fig. 2(c')), can point to the coexistence of RA and reverted austenite in the heat-treated samples [2,28].

According to the EBSD results, the vertical (as-built) specimens had slightly larger grains than the horizontal (as-built) ones (Fig. 3). This difference in the grain size can be attributed to the higher number of material layers required to manufacture the vertical samples. The higher number of deposited layers exposes the sample to more thermal energy and heat accumulation during the AM. Ultimately, higher heat accumulation in the vertical samples than the horizontal ones can increase the prior (parent) austenite grain (PAG) size [9]. Higher PAG size decreases the resistance of austenite against austenite/martensite interface movement and increases the Ms temperature [1,29]. Consequently, the vertical samples were expected to have lower austenite contents and coarser martensitic morphologies than the horizontal ones.

Regarding the heat-treated CX, according to the dilatometry data, during the annealing stage of the heat treatment, the vertical specimens experienced a higher rate of austenitization than the horizontals (Fig. 4 (b)). This difference in the transformation kinetics can also be attributed to the different sizes of the martensitic features of the vertical (as-built) and horizontal (as-built) samples. The higher austenitization rate provided the austenite grains in the vertical samples with more time to grow. Accordingly, the vertical samples had even larger PAGs at the end of the solution annealing. The larger PAGs resulted in a higher Ms temperature in the annealed vertical specimens than the horizontals. Consequently, the final average grain size difference between the vertical and horizontal samples became even more prominent after the heat treatment, and the austenite contents of the vertical (heat-treated) specimens were generally still smaller than the horizontal (heat-treated) specimens (Table 4).
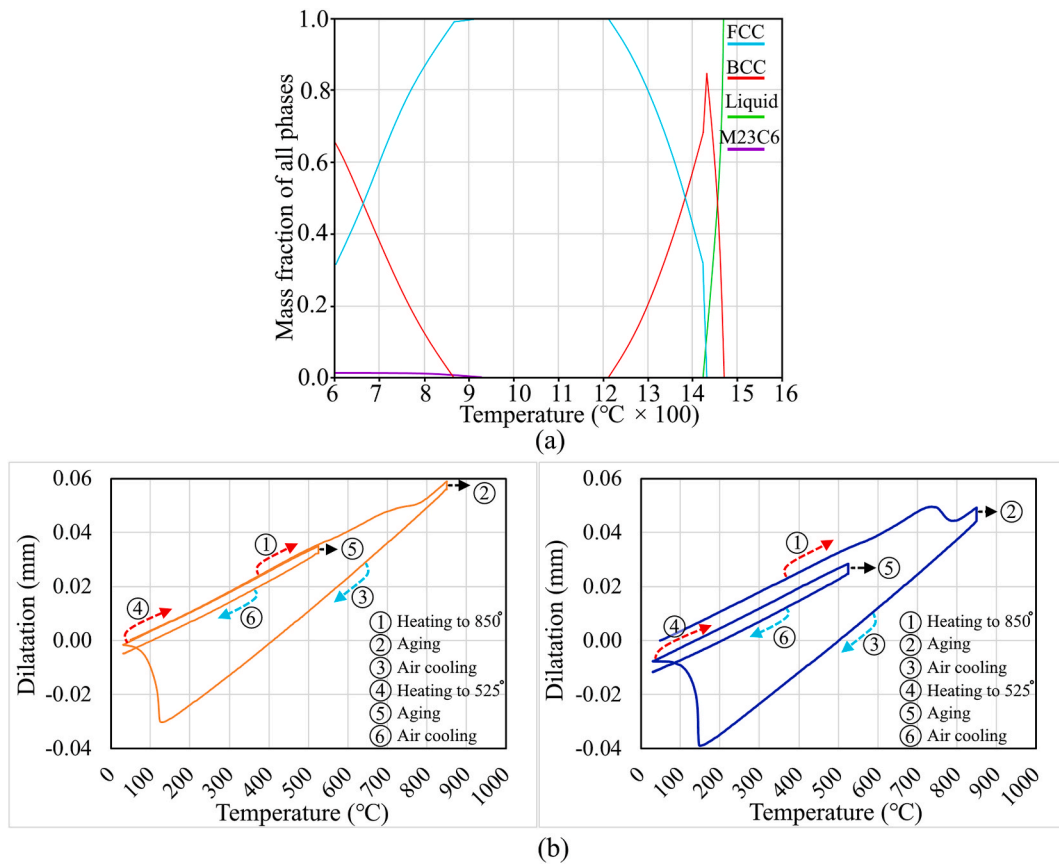
Fig. 4. (a) Expected phases in L-PBF CX during its heating cycle, according to the calculations by ThermoCalc software, and (b) the results of the dilatometry analysis from the horizontal (left) and vertical (right) specimens.
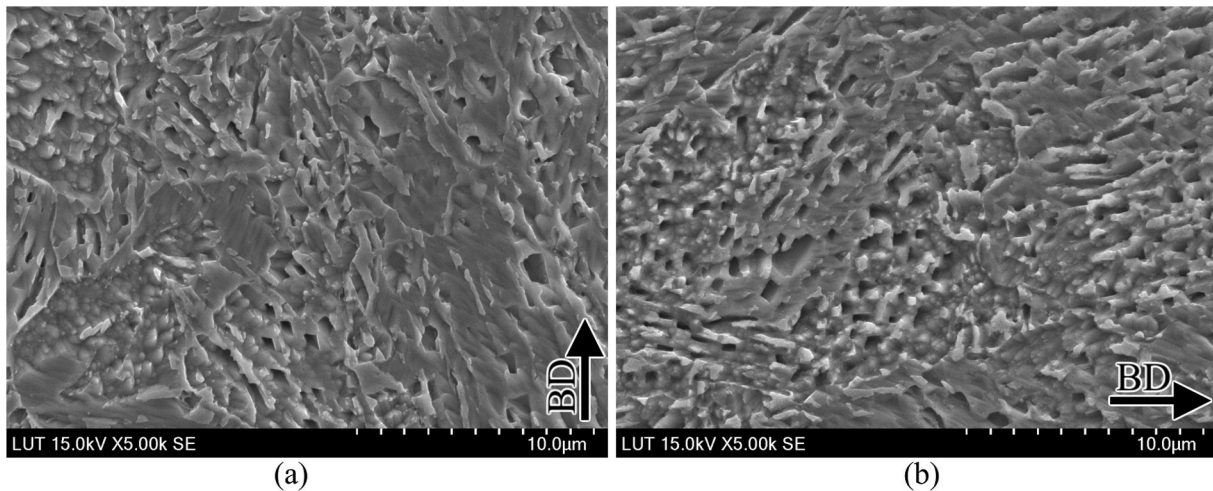

Fig. 5. SEM micrographs of the heat-treated samples in their building planes: (a) horizontal and (b) vertical specimens.

After the heat treatment, as shown in Fig. 5, L-PBF CX consisted of higher amounts of lath martensite than its as-built condition, regardless of its BD. This change of LM to DM ratio can be attributed to the more moderate heating and cooling courses of the heat treatment compared to the AM process [14]. The heat treatment also made the texture of L-PBF CX weaker, regardless of its BD. The texture weakening can be attributed to the recrystallization and stochastic formation of martensite laths during the austenitization annealing and quenching. Consequently, the heat-treated microstructure was not under the influence of the strong thermal gradient of L-PBF anymore, and, ultimately, its texture was weaker than that of the as-built microstructure [10,13]. Finally, nano-scale β-NiAl precipitates in the heat-treated microstructure were expected as the main result of the aging stage. These coherent particles with an average size of 20 nm are the main strengthening feature in the heat-treated L-PBF CX. However, due to the limitation associated with the accuracies of SEM and FE-SEM approaches used in the current study, this average size cannot be attributed to all the strengthening particles present in L-PBF CX. Hadadzadeh et al. [5] investigated heat-treated L-PBF CX using TEM and estimated the true average size of β-NiAl particles to be 5.6 nm. Consequently, since the critical size of β-NiAl is
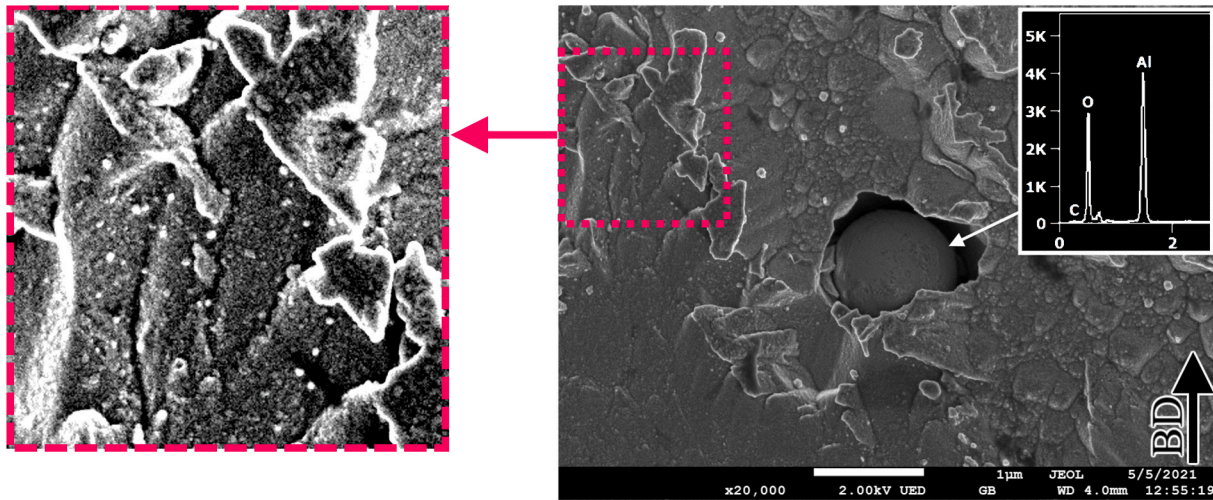
Fig. 6. FE-SEM image of the precipitates from a horizontal (heat-treated) specimen.

Table 5
Surface roughness values of L-PBF CX.

Surface condition, BD, and post-processing	Ra (μm)	Rz (μm)
Raw horizontal (as-built)	4	34
Machined horizontal (as-built)	1	5
Machined horizontal (heat-treated)	1	5
Raw vertical (as-built)	3	24
Raw vertical (heat-treated)	3	21
Machined vertical (as-built)	1	5
Machined vertical (heat-treated)	1	6

7.6 nm, these particles are expected to contribute to the strengthening primarily via particle shearing rather than Orowan (looping) mechanism [5,15].

4.2. Surface quality and residual stress values

Building orientation commonly affects the surface quality of L-PBF metals [25,26]. However, according to Table 5, this parameter did not significantly affect the surface roughness of L-PBF CX. This insensitivity might be attributed to the characteristics of molten CX (e.g., wetting angle and viscosity). However, further study is required regarding this matter. In addition, mechanical machining decreased the surface roughness, as expected, and applied compressive residual stress on the specimens (Fig. 7(a)). Regarding the residual stress, BD also had a significant effect on this parameter, and the raw vertical (as-built) sample had tensile residual stress, while the residual stress of the raw horizontal (as-built) sample was compressive.

The different types of residual stresses in the samples with dissimilar BDs can be attributed to the different scanning times, the total number of required deposited layers, and aspect ratios of the vertical samples than those of the horizontal ones [24]. Furthermore, the tensile residual stress of the raw vertical (as-built) specimens increased from bottom to top due to the heat accumulation and the increasing number of deposited layers during the AM process [9]. Finally, heat treatment decreased and normalized the residual stress values, regardless of specimen type. Such an effect for the heat treatment on the residual stress values was expected since the procedure included an annealing stage [24].

Finally, austenite to martensite transformation is commonly accompanied by residual stress due to the changes in the lattice parameters. Consequently, externally applied residual stresses are also supposed to influence the martensite to austenite phase transformation [30]. However, residual stresses induced in the bent samples described in Section 3.2 had no significant effect on the post-heat treatment

microstructure of L-PBF CX, regardless of its BD and residual stress type. This immunity of the heat-treated L-PBF CX to the effects of residual stress on the microstructure might be attributed to stress relaxation at the initial stages of the annealing. However, determining the main reason behind such material behavior requires more detailed research on the interactions between residual stress and microstructure in future studies.

4.3. Hardness and notch toughness

The hardness in the as-built L-PBF CX had a uniform distribution, and BD did not affect the hardness. Thus, the most significant strengthening factors regarding the hardness of as-built L-PBF CX can be related to the average effective grain size and dislocation densities in L-PBF CX. This attribution is due to that these parameters are not significantly different between horizontal and vertically made samples. Furthermore, no strengthening precipitates were detected in the as-built specimens. After the heat treatment, hardness increased uniformly, regardless of the BD. The increase was due to β-NiAl precipitates. The uniform hardness increase in the building plane and scanning plane of all samples can result from the homogeneous distribution of the coherent nanoparticles throughout the material [14], regardless of its BD or measurement location. Finally, residual stresses induced in the bent specimens did not cause a significant difference in the hardness values after the heat treatment. This material behavior was expected since the post-heat treatment microstructures of the bent specimens were similar to those of the other samples, and hardness in metals is commonly recognized to be highly dependent upon their microstructures [24,25].

The hardness and toughness of steel typically are reversely related, and an increase in hardness decreases the toughness [7,31]. Consequently, the notch toughness of the heat-treated L-PBF CX was significantly lower than that of the as-built L-PBF CX. In addition, compared to the as-built specimens, heat-treated L-PBF CX experienced a relatively brittle fracture considering its significantly low SFA values. The significant change in the notch toughness and fracture mechanism can be attributed to the precipitation of β-NiAl nanoparticles due to aging treatment. However, similar to hardness, BD did not significantly affect the notch toughness.

4.4. Quasi-static mechanical properties of as-built L-PBF CX

Strength levels of L-PBF metals under quasi-static tensile loads are typically higher for horizontally made samples than verticals due to numerous reasons depending on the material [24–26]. Regarding L-PBF CX, it is possible to understand the different properties of vertical and
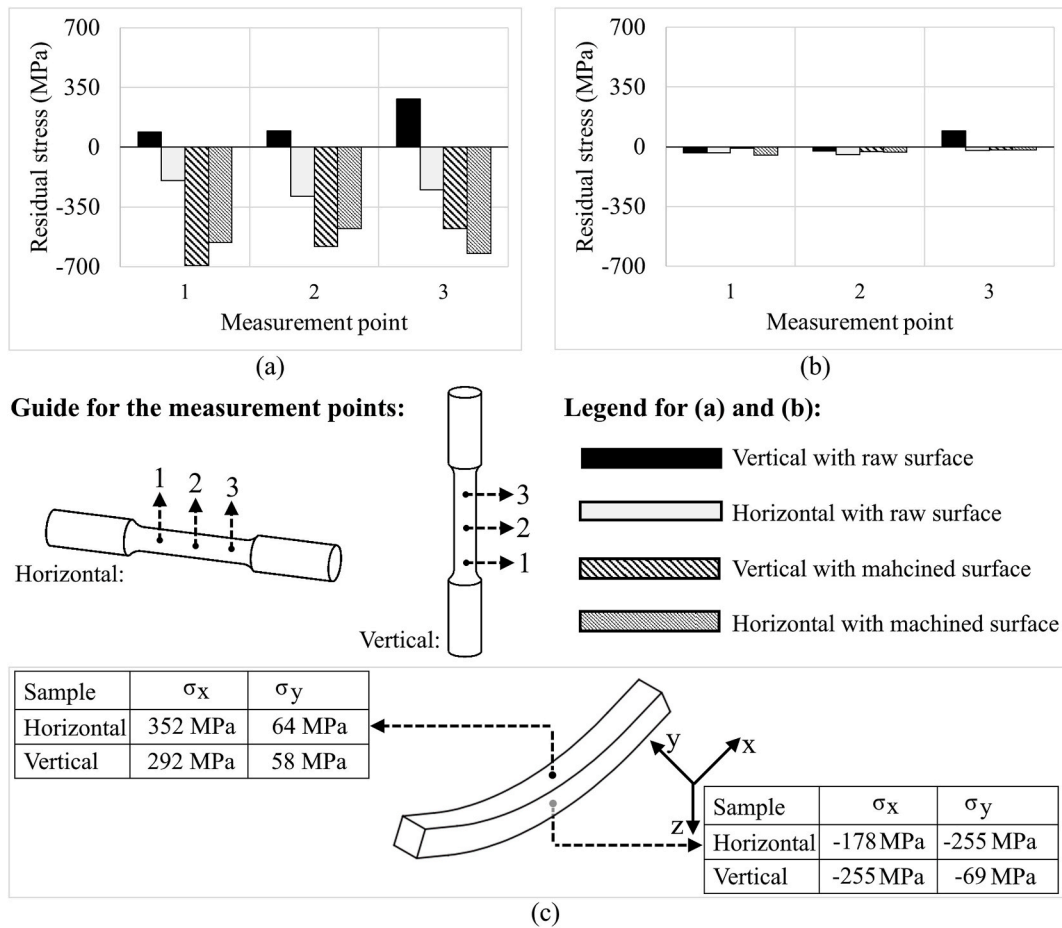
Fig. 7. Residual stress values of the (a) as-built and (b) heat-treated specimens; (c) local residual stress values of the bent samples according to their building orientation.

Table 6
Numerical data from the EBSD analysis of the bent samples after their heat treatment.

Sample BD (analysis location)	LAGBs fraction (1° - 5°)	LAGBs fraction (5° - 15°)	HAGBs fraction (> 15°)	Area fraction of austenite	Area fraction of martensite
Horizontal (inside curvature)	22.6% (0.5 cm)	14.0% (0.3 cm)	63.4% (1.4 cm)	3.3%	96.7%
Horizontal (outer curvature)	22.8% (0.5 cm)	13.7% (0.3 cm)	63.5% (1.3 cm)	2.3%	97.7%
Vertical (inside curvature)	24.4% (0.6 cm)	14.3% (0.3 cm)	61.3% (1.4 cm)	2.5%	97.5%
Vertical (outer curvature)	25.8% (0.6 cm)	14% (0.3 cm)	60.3% (1.4 cm)	2.7%	97.3%

Table 7
Hardness values of L-PBF CX according to its DB and measurement planes.

Type of BD and post-processing	Hardness in the building plane (HV)	Hardness in the scanning plane (HV)
Horizontal (as-built)	318	336
Horizontal (heat-treated)	467	462
Vertical (as-built)	324	322
Vertical (heat-treated)	477	472

horizontal samples by evaluating the effective strengthening mechanisms in this material. For a precipitation hardening martensitic steel such as L-PBF CX, yield strength (σ_{yield}) can be broken down into four different components: strength increments due to grain boundaries or effective grain size (σ_{HAGBs}), dislocations ($\sigma_{dislocations}$), precipitates and second particles ($\sigma_{precipitates}$), and texture ($\sigma_{texture}$) [5,15]. It should be noted that in the as-built L-PBF CX, no strengthening particle was detected ($\sigma_{precipitates} \approx 0$). Thus, grain boundaries, dislocation network, and texture are expected to be the most influential factors affecting the

quasi-static strength of the material.

The average effective grain size in the vertical samples was slightly higher than the horizontal ones, as shown in Fig. 3. This difference can cause a slight decrease in the yield strength of the vertical specimens. However, as schematically shown in Supplementary Figure 13, during L-PBF, PAGs initially tend to grow toward the BD, which is parallel to the maximum thermal gradient. This tendency results in some elongated grains aligned along the BD. Consequently, due to the inhomogeneous microstructure, applied external loads might interact with different numbers of HAGBs depending on their directions. Thus, external loads applied on the vertical specimens, in which the LA and BD are parallel, interact with fewer HAGBs. This phenomenon can further decrease the strengthening effect of the HAGBs in the vertical samples and increase the difference between the horizontal and vertical samples in terms of σ_{HAGBs}.

$\sigma_{dislocations}$ depends on the densities of the dislocations trapped in the martensitic laths or dendrites. The high dislocation densities result from ultra-high cooling rates associated with L-PBF and microstructural strains accompanying martensite formation [31,32]. However,
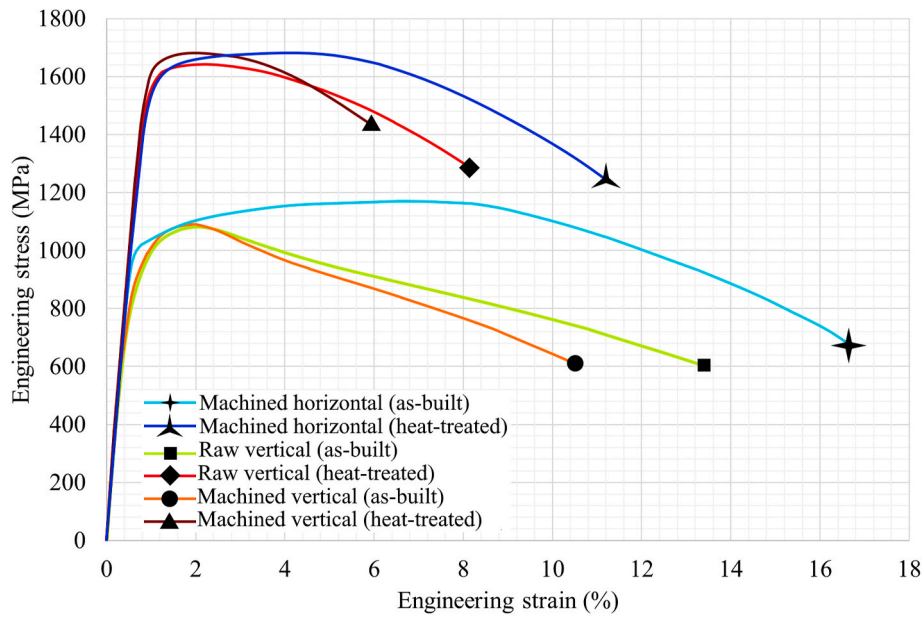
Fig. 8. Engineering stress-strain curves of the specimens.

Table 8
Quasi-static properties of L-PBF CX.

Sample type	0.2% Yield strength (MPa)	Tensile strength (MPa)	**Elongation (%)**	Tangent modulus (GPa)
Machined horizontal (as-built)	1006.0	1170.4	16.6	197.8
Machined horizontal (heat-treated)	1533.4	1680.1	11.2	188.9
Raw vertical (as-built)	899.3	1081.2	13.3	175.7
Raw vertical (heat-treated)	1556.3	1641.5	8.1	194.5
Machined vertical (as-built)	919.2	1090.2	10.5	181.1
Machined vertical (heat-treated)	1600.9	1682.7	5.9	203.6

Table 9
Notch toughness values of the specimens.

Sample type	**Horizontal (as-built)**	**Horizontal (heat-treated)**	**Vertical (as-built)**	**Vertical (heat-treated)**
Noth toughness (J)	139.0	29.0	128.0	22.0
SFA (%)	67.3	17.5	65.9	18.0

repetitive heating and cooling cycles and layers remelting during L-PBF can cause in-situ local tempering in some regions throughout the microstructure and result in autotempered martensites with lower dislocation densities [9]. The presence of martensitic features with lower local dislocation densities seems more frequent and possible in vertical samples since these specimens are made of significantly more deposited layers and, consequently, endure more repetitive thermal cycles than horizontal samples. Consequently, $\sigma_{\text{dislocations}}$ is more likely to be smaller in the vertical samples compared to the horizontal ones [1,

4]. However, it should be noted that in this study, unlike in [4], the density of LAGBs attributed to the dislocations for the vertical sample was not significantly lower than the horizontal specimen (Table 4). This controversy can be attributed to the methods used to perform the measurements. In Refs. [1,4], as a more precise and sophisticated apparatus than EBSD, TEM has been used to measure the dislocation densities.

Regarding the σ_{texture}, as shown in Section 3.1, although both horizontal and vertical samples had weakened textures in their as-built condition with weak tendencies toward <111> and <110> for their martensitic background and RA islands, respectively, the alignment of these weak textures with respect to the LA is different in the vertical and horizontal specimens. The different alignments can result in different Schmid factors and σ_{texture} contributions in the yield strength since σ_{texture} is equal to the ratio of the critical resolved shear stress of crystals (grains), ≈ 92 MPa for CX, to their Schmid factors [15]. However, considering the generally weak texture of L-PBF CX, the role of σ_{texture} in the material strength might be minor compared to σ_{HAGBs} and $\sigma_{\text{dislocations}}$, and clarification of this issue requires further research.

L-PBF CX showed lower degrees of anisotropy in its strength levels than solid solution L-PBF steels, e.g., L-PBF 316L in [19], as shown in Table 10. The higher tolerance of L-PBF CX against such anisotropy can be due to the numerous active strengthening mechanisms in this material. Unlike a solid solution AM metal, the strength of CX does not rely on only one mechanism, e.g., grain boundary strengthening or solid solution atoms. Thus, leveraging simultaneously from different strengthening mechanisms, i.e., σ_{HAGBs}, $\sigma_{\text{dislocations}}$, $\sigma_{\text{precipitates}}$, and σ_{texture}, might

Table 10
Comparison of anisotropies between L-PBF CX and L-PBF 316L.

Material	L-PBF CX	L-PBF 316L [19]
Yield strength for the machined horizontal (as-built)	1006 MPa	546 MPa
Yield strength for the machined vertical (as-built)	919 MPa	475 MPa
Tensile strength for the machined horizontal (as-built)	1170 MPa	654 MPa
Tensile strength for the machined vertical (as-built)	1090 MPa	569 MPa
Anisotropy in the yield strength	9.4%	14.9%
Anisotropy in the tensile strength	7.3%	14.9%

result in these mechanisms normalizing the influence of each other in the horizontal and vertical samples made of L-PBF CX and decreasing its anisotropic behavior regarding the strength.

Mechanical machining did not have a significant effect on the yield and tensile strengths of L-PBF CX. This indifference can be attributed to the good surface quality of raw L-PBF CX (Ra ≈ 3 μm). However, the machined samples had lower elongation values compared to the raw specimens. Furthermore, the horizontal samples had higher elongations than the vertical specimens, regardless of the post-processing condition. The higher ductility of the horizontal specimens seems controversial since, in AM metals, lower strength limits of vertically made samples are typically accompanied by higher elongations.

The controversy can be caused by the higher amount of austenite in the horizontal samples, regardless of their post-processing condition, as shown in Table 4. The presence of austenite in martensite generally improves the ductility and toughness of martensitic steels [33–35]. Finally, the heat treatment resulted in more organized and uniform martensitic laths, weaker textures, and consistent distributions of β-NiAl particles throughout the microstructures in both horizontal and vertical samples. Subsequently, the precipitation caused a significant increase in $\sigma_{precipitates}$, regardless of the BD, and strengthened the material. In addition, weaker textures for both heat-treated horizontal and heat-treated vertical samples (compared to their as-built versions) eliminated the difference in their $\sigma_{texture}$ values. The summation of these factors decreased the difference in the strength levels for the heat-treated horizontal and vertical specimens.

Regarding the different strain hardening behaviors, the three-stage hardening of the vertical (as-built) samples can be attributed to their RA. As the second stage of strain hardening, the hardening recovery is possible in austenitic microstructures with a dominant <110> texture towards their LA. The recovery occurs in such austenites due to strain-induced austenite to martensite transformation or deformation twinnings, depending on the stacking fault energy of the austenite [19,36, 37]. Therefore, although L-PBF CX is not austenitic, the RA with <110> texture towards the LA in the vertical (as-built) samples might have caused the slight strain hardening recovery in the three-stage hardening behavior of these samples. However, such hardening behavior was not observed in the heat-treated specimens since the post-heat treatment textures were even further weakened.

5. Conclusions

L-PBF CX, as a precipitation hardening martensitic stainless steel, imparts a favorable combination of strength, ductility, and corrosion resistance for industrial applications. In this study, CX was subjected to microstructural evaluations and mechanical tests. Furthermore, the efficiency of the optimized heat treatment for L-PBF CX was also studied. According to the results, the following points can be drawn:

- L-PBF CX had a combination of lath and dendritic martensites accompanied with sporadic islands of austenite along its high-angle grain boundaries as the as-built microstructure. Heat treatment resulted in more lath-like martensitic morphologies and uniform precipitation of β-NiAl nanoparticles.
- Horizontally manufactured L-PBF CX generally had higher austenite contents than vertical samples, regardless of the post-processing condition. The lower austenite contents in the vertical samples can be attributed to the higher heat accumulations in their AM process.
- The modified heat treatment used in this study to improve the mechanical properties of L-PBF CX proved to be as effective as the more energy- and time-consuming treatments used in the prior studies from the literature.
- As-built L-PBF CX had anisotropic behavior under quasi-static uni-axial tensile loads. Similar to other AM metals, the anisotropy can be attributed to the different alignments of weak links (spots) or microstructural features in the horizontal and vertical samples

[24–26]. However, compared to 316L as a solid solution AM metal, L-PBF CX showed lower degrees of anisotropy in its strength levels. The higher tolerance of L-PBF CX against such anisotropy can be due to the numerous active strengthening mechanisms in this material.
- Horizontally made L-PBF CX had higher elongation to failure values than the vertical samples, regardless of post-processing. The higher ductility can be attributed to the higher austenite contents of the horizontal samples.
- Building orientation did not affect the hardness and notch toughness, but heat treatment significantly increased the hardness and decreased the notch toughness of L-PBF CX.
- Compared to other AM steels, building orientation did not significantly influence the surface quality of L-PBF CX.

Finally, although L-PBF CX has been the subject of numerous recent studies, the effect of austenite content on its mechanical behavior and corrosion resistance should be more thoroughly investigated. Further, the fatigue characteristics of L-PBF CX have yet to be understood. Considering the high potential of this material for industrial applications requiring simultaneous high levels of strength and corrosion resistance accompanied by acceptable ductility, in addition to the knowledge gaps mentioned in this research, comprehensively understanding the full capabilities of CX and its behavior under different conditions has a long way to achieve.

Data availability statement

The raw/processed data required to reproduce these findings can be obtained upon request from the corresponding author.

CRediT authorship contribution statement

Shahriar Afkhami: Conceptualization, Methodology, Software, Investigation, Writing – original draft, Writing – review & editing, Visualization. **Vahid Javaheri:** Conceptualization, Methodology, Investigation, Validation, Writing – review & editing. **Edris Dabiri:** Conceptualization, Methodology, Validation, Writing – original draft, Writing – review & editing. **Heidi Piili:** Writing – review & editing, Supervision, Funding acquisition. **Timo Björk:** Conceptualization, Writing – review & editing, Supervision, Funding acquisition.

Declaration of competing interest

The authors declare that they have no known competing financial interests or personal relationships that could have appeared to influence the work reported in this paper.

Acknowledgment

References

[1] A. Shahriari, L. Khaksar, A. Nasiri, A. Hadadzadeh, B.S. Amirkhiz, M. Mohammadi, Microstructure and corrosion behavior of a novel additively manufactured maraging stainless steel, Electrochim. Acta 339 (2020) 135925, https://doi.org/10.1016/j.electacta.2020.135925.
[2] A. Shahriari, M. Ghaffari, L. Khaksar, A. Nasiri, A. Hadadzadeh, B.S. Amirkhiz, M. Mohammadi, Corrosion resistance of 13wt.% Cr martensitic stainless steels:

additively manufactured CX versus wrought Ni-containing AISI 420, Corrosion Sci. 184 (2021) 109362, https://doi.org/10.1016/j.corsci.2021.109362.

[3] M. Sanjari, A. Hadadzadeh, A. Shahriairi, S. Tamimi, H. Pirgazi, B.S. Amirkhiz, L. Kestens, M. Mohammadi, On the effect of building direction on the microstructure and grain morphology of a selective laser melted maraging stainless steel, in: Miner. Met. Mater. Ser., Springer, 2020, pp. 285–295, https://doi.org/10.1007/978-3-030-36296-6_27.

[4] M. Sanjari, A. Hadadzadeh, H. Pirgazi, A. Shahriari, B.S. Amirkhiz, L.A.I. Kestens, M. Mohammadi, Selective laser melted stainless steel CX: role of built orientation on microstructure and micro-mechanical properties, Mater. Sci. Eng. 786 (2020) 139365, https://doi.org/10.1016/j.msea.2020.139365.

[5] A. Hadadzadeh, A. Shahriari, B.S. Amirkhiz, J. Li, M. Mohammadi, Additive manufacturing of an Fe–Cr–Ni–Al maraging stainless steel: microstructure evolution, heat treatment, and strengthening mechanisms, Mater. Sci. Eng. 787 (2020) 139470, https://doi.org/10.1016/j.msea.2020.139470.

[6] L. Kučerová, K. Burdová, Š. Jeníček, I. Chena, Effect of solution annealing and precipitation hardening at 250 °C–550 °C on microstructure and mechanical properties of additively manufactured 1.2709 maraging steel, Mater. Sci. Eng. 814 (2021) 141195, https://doi.org/10.1016/J.MSEA.2021.141195.

[7] P. Bajaj, A. Hariharan, A. Kini, P. Kürnsteiner, D. Raabe, E.A. Jägle, Steels in additive manufacturing: a review of their microstructure and properties, Mater. Sci. Eng. 772 (2020) 138633, https://doi.org/10.1016/j.msea.2019.138633.

[8] H. Pirgazi, M. Sanjari, S. Tamimi, B. Shalchi Amirkhiz, L.A.I. Kestens, M. Mohammadi, Texture evolution in selective laser melted maraging stainless steel CX with martensitic transformation, J. Mater. Sci. 56 (2021) 844–853, https://doi.org/10.1007/s10853-020-05290-2.

[9] F. Marin, A.F. de Souza, C.H. Ahrens, L.N.L. de Lacalle, A new hybrid process combining machining and selective laser melting to manufacture an advanced concept of conformal cooling channels for plastic injection molds, Int. J. Adv. Manuf. Technol. 113 (2021) 1561–1576, https://doi.org/10.1007/s00170-021-06720-4.

[10] R. Palad, Y. Tian, K. Chadha, S. Rodrigues, C. Aranas, Microstructural features of novel corrosion-resistant maraging steel manufactured by laser powder bed fusion, Mater. Lett. 275 (2020) 128026, https://doi.org/10.1016/j.matlet.2020.128026.

[11] A. Hadadzadeh, B.S. Amirkhiz, J. Li, M. Mohammadi, Microstructure evolution in direct metal laser sintered Corrax maraging stainless steel, in: Miner. Met. Mater. Ser., Springer International Publishing, 2019, pp. 455–462, https://doi.org/10.1007/978-3-030-05861-6_42.

[12] H. Asgari, M. Mohammadi, Microstructure and mechanical properties of stainless steel CX manufactured by Direct Metal Laser Sintering, Mater. Sci. Eng. 709 (2018) 82–89, https://doi.org/10.1016/j.msea.2017.10.045.

[13] Y. Tian, R. Palad, C. Aranas, Microstructural evolution and mechanical properties of a newly designed steel fabricated by laser powder bed fusion, Addit. Manuf. 36 (2020) 101495, https://doi.org/10.1016/j.addma.2020.101495.

[14] J. Zhang, M. Wang, L. Niu, J. Liu, J. Wang, Y. Liu, Z. Shi, Effect of process parameters and heat treatment on the properties of stainless steel CX fabricated by selective laser melting, J. Alloys Compd. 877 (2021) 160062, https://doi.org/10.1016/j.jallcom.2021.160062.

[15] D. Dong, C. Chang, H. Wang, X. Yan, W. Ma, M. Liu, S. Deng, J. Gardan, R. Bolot, H. Liao, Selective laser melting (SLM) of CX stainless steel: theoretical calculation, process optimization and strengthening mechanism, J. Mater. Sci. Technol. 73 (2021) 151–164, https://doi.org/10.1016/J.JMST.2020.09.031.

[16] EOS, EOS StainlessSteel CX material data sheet. https://www.eos.info/03_system-related-assets/material-related-contents/metal-materials-and-examples/metal-material-datasheet/stainlesssteel/material_datasheet_eos_stainlesssteel_cx_premium_en_web.pdf, 2021. (Accessed 22 April 2021).

[17] P. Yadav, V.K. Singh, T. Joffre, O. Rigo, C. Arvieu, E. Le Guen, E. Lacoste, Inline drift detection using monitoring systems and machine learning in selective laser melting, Adv. Eng. Mater. 22 (2020) 2000660, https://doi.org/10.1002/adem.202000660.

[18] A.B. Spierings, M. Schneider, R. Eggenberger, Comparison of density measurement techniques for additive manufactured metallic parts, Rapid Prototyp. J. 17 (2011) 380–386, https://doi.org/10.1108/13552541111156504.

[19] S. Afkhami, M. Dabiri, H. Piili, T. Björk, Effects of manufacturing parameters and mechanical post-processing on stainless steel 316L processed by laser powder bed fusion, Mater. Sci. Eng. 802 (2021) 140660, https://doi.org/10.1016/j.msea.2020.140660.

[20] G.F. Vander Voort, Volume 9: metallographic and microstructures, in: ASM Handb., ASM International, 2004, p. 1184.

[21] ASTM Standard E8/E8M, Tension Testing of Metallic Materials, ASTM Int., 2016, pp. 1–27, https://doi.org/10.1520/E0008_E0008M-16A.

[22] ASTM International, ASTM E23 − 18, Standard Test Methods for Notched Bar Impact Testing of Metallic Materials, ASTM Int., 2018, pp. 1–26, https://doi.org/10.1520/E0023-18.

[23] M. Dabiri, M. Lindroos, T. Andersson, S. Afkhami, A. Laukkanen, T. Björk, Utilizing the theory of critical distances in conjunction with crystal plasticity for low-cycle notch fatigue analysis of S960 MC high-strength steel, Int. J. Fatig. 117 (2018), https://doi.org/10.1016/j.ijfatigue.2018.07.042.

[24] S. Afkhami, M. Dabiri, S.H. Alavi, T. Björk, A. Salminen, S. Habib Alavi, T. Björk, A. Salminen, Fatigue characteristics of steels manufactured by selective laser melting, Int. J. Fatig. 122 (2019) 72–83, https://doi.org/10.1016/j.ijfatigue.2018.12.029.

[25] S. Afkhami, H. Piili, A. Salminen, T. Björk, Effective parameters on the fatigue life of metals processed by powder bed fusion technique: a short review, Procedia Manuf 36 (2019) 3–10, https://doi.org/10.1016/j.promfg.2019.08.002.

[26] H. Fayazfar, M. Salarian, A. Rogalsky, D. Sarker, P. Russo, V. Paserin, E. Toyserkani, A critical review of powder-based additive manufacturing of ferrous alloys: process parameters, microstructure and mechanical properties, Mater. Des. 144 (2018) 98–128, https://doi.org/10.1016/J.MATDES.2018.02.018.

[27] S. Kou, Welding Metallurgy, John Wiley & Sons, Inc., Hoboken, NJ, USA, 2002, https://doi.org/10.1002/0471434027.

[28] F. Qian, W.M. Rainforth, The formation mechanism of reverted austenite in Mn-based maraging steels, J. Mater. Sci. 548 (54) (2019) 6624–6631, https://doi.org/10.1007/S10853-019-03319-9, 2019.

[29] C. Celada-Casero, C. Kwakernaak, J. Sietsma, M.J. Santofimia, The influence of the austenite grain size on the microstructural development during quenching and partitioning processing of a low-carbon steel, Mater. Des. 178 (2019) 107847, https://doi.org/10.1016/j.matdes.2019.107847.

[30] H.K.D.H. Bhadeshia, Material factors, in: Handb. Residual Stress Deform. Steel, ASM International, Materials Park, Ohio, 2002, pp. 3–11.

[31] S. Gorsse, C. Hutchinson, M. Gouné, R. Banerjee, Additive manufacturing of metals: a brief review of the characteristic microstructures and properties of steels, Ti-6Al-4V and high-entropy alloys, Sci. Technol. Adv. Mater. 18 (2017) 584, https://doi.org/10.1080/14686996.2017.1361305.

[32] S. Cheruvathur, E.A. Lass, C.E. Campbell, Additive manufacturing of 17-4 PH stainless steel: post-processing heat treatment to achieve uniform reproducible microstructure, 68 (n.d.). https://doi.org/10.1007/s11837-015-1754-4..

[33] K. Zhang, M. Zhang, Z. Guo, N. Chen, Y. Rong, A new effect of retained austenite on ductility enhancement in high-strength quenching–partitioning–tempering martensitic steel, Mater. Sci. Eng. 528 (2011) 8486–8491, https://doi.org/10.1016/J.MSEA.2011.07.049.

[34] N. Hirakawa, K. Tsuboi, Y. Yoshimura, E. Ishimaru, Effect of Retained Austenite Phase on Ductility of Martensitic Stainless Steel, ((n.d.)).

[35] E. De Moor, S. Lacroix, A.J. Clarke, J. Penning, J.G. Speer, Effect of retained austenite stabilized via quench and partitioning on the strain hardening of martensitic steels, Metall. Mater. Trans. 39 (2008) (2008) 2586–2595, https://doi.org/10.1007/S11661-008-9609-Z, 3911.

[36] Y.M. Wang, T. Voisin, J.T. McKeown, J. Ye, N.P. Calta, Z. Li, Z. Zeng, Y. Zhang, W. Chen, T.T. Roehling, R.T. Ott, M.K. Santala, P.J. Depond, M.J. Matthews, A. V. Hamza, T. Zhu, Additively manufactured hierarchical stainless steels with high strength and ductility, Nat. Mater. 17 (2018) 63–70, https://doi.org/10.1038/NMAT5021.

[37] X. Wang, J.A. Muñiz-Lerma, M. Attarian Shandiz, O. Sanchez-Mata, M. Brochu, Crystallographic-orientation-dependent tensile behaviours of stainless steel 316L fabricated by laser powder bed fusion, Mater. Sci. Eng. 766 (2019) 138395, https://doi.org/10.1016/j.msea.2019.138395.